NSRRC-J05146(2016)

THE JOURNAL OF PHYSICAL CHEMISTRY

Article

pubs.acs.org/JPCC

# Size Effect of Atomic Gold Clusters for Carbon Monoxide Passivation at $Ru_{core}$–$Pt_{shell}$ Nanocatalysts

Tsan-Yao Chen,*[,†] Yu-Ting Liu,*[,‡] Jeng Han Wang,[§] Guo-Wei Lee,[∥] Po-Wei Yang,[†] and Kuan-Wen Wang[⊥]

[†]Department of Engineering and System Science, National Tsing Hua University, Hsinchu 30013, Taiwan

[‡]Department of Soil and Environmental Science, National Chung Hsing University, Taichung 402, Taiwan;

[§]Department of Chemistry, National Taiwan Normal University, Taipei 106, Taiwan

[∥]Department of Physics, National Tsing Hua University, Hsinchu 30013, Taiwan

[⊥]Institute of Materials Science and Engineering, National Central University, Taoyuan City, Taiwan

Supporting Information

ABSTRACT: The surface of $Pt_{shell}$–$Ru_{core}$ nanocatalysts was modified with an atomic-scaled Au cluster of different sizes by a polyol reduction technique using sequence and composition control. Our results, combining the structure, surface chemical analysis, and density functional theory calculation, elucidate that these clusters reduced the oxidation current of carbon monoxide to a maximum extent of ~53%; consequently, the anti-CO poisoning factor of the NCs was doubled by increasing the Au/Pt ratios from 0 to 15 at%. Such substantial improvement is caused by steric shielding and the electron localization field that reject the sorption of electronegative ligands/molecules at the NC surface by Au clusters. Most importantly, this work clarifies the mechanistic insights of the charge relocation at core–shell nanoparticles by subnanoscaled cluster intercalation and the impacts of cluster size for the chemical durability of catalysts in fuel cell applications.

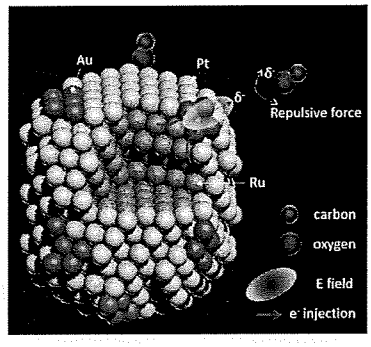


## INTRODUCTION

Carbon monoxide passivation is one of the most influential factors among all types of physiochemical reactions on nanocatalysts (NCs) (i.e., metal dissolution, oxidation formation, surface polarization, and interparticle agglomeration of NCs) in the fuel cell lifetime.[1] Compared with other degradation modes having slow kinetics,[1] chemical passivation occurs in radical ways (just in a few seconds) to drop the device power by more than 50%.[2,3] On the basis of heterogeneous catalysis theory, surface passivation can be suppressed by modifying the local electronic structure around the reaction sites at the NC surface. Increasing the identity and number of hydrophilic heteroatoms has proved to be an effective strategy for preventing this weakness. Such a strategy mainly relies on fundamental heteroatomic/hetero-junction electron relocation pathways (i.e., bifunctional mechanism, the ligand effects, and the lattice strain in the near surface region)[4−6] and can be achieved by growing the nanoparticles into different configurations.

The core–shell structured NCs (in particular the semi-coherent interface) possess outstanding redox performance among electrochemical catalysts because the heterojunction interface can serve as an electron injection channel to evacuate or inject electrons in the surface region.[7] These electron redistributions effectively facilitate redox kinetics against electrochemical reagents (for example, the CO oxidation in fuel reformate systems at room temperature[1,2,8]) which reduce the lifetime of chemisorption residuals and thus preserve the structure stability of NCs in operando fuel cells.[1,9] Combining experimental results and theoretical first principle density functional theory (DFT) calculation,[5] the direction and strength of such interfacial charge relocation are dominated by the identity and thickness of the shell crystal and can only propagate by ~1.0 nm at a maximum (i.e., ~3–4 atomic layers in most cases).[5,10] These advantages seem to rationalize the optimum design for fuel cell NCs. However, considering their selectivity and durability to chemical species, a state of the art NC technique is still far from being applied at industrial scale.

Durability and activity for decomposing carbonaceous fuel molecules are the most essential criteria for the application of NCs particularly in long-term operando fuel cells under industrial standards. Among conventional approaches (including the growth of alloy, cluster-in-cluster, core–shell, and Janus structures), the core–shell structure is believed to be the most promising geometry to meet these criteria especially for electrochemical stability and activity of NCs against CO poisoning. Intercalating heteroatoms at the surface will reinforce not only the chemical but also the physical structure of the NCs in long-term redox reactions (such as oxygen reduction and

Received: January 25, 2016
Revised: March 13, 2016
Published: March 16, 2016

ACS Publications © 2016 American Chemical Society



DOI: 10.1021/acs.jpcc.6b00801
J. Phys. Chem. C 2016, 120, 7621−7628

methanol electrooxidation). Although robust synthetic scenarios have been demonstrated, little work has been conducted with clear rationales for the mechanisms behind the NC properties. Our previous works successfully demonstrated the synthesis of surface gold clusters in atomic scale heterojunctions for stabilizing the chemical and geometrical structures of $Pt_{shell}$–$Ru_{core}$ NCs ($Pt_S/Ru_C$ NCs) in methanol oxidation reactions (MOR).[11] In this study, we disclose the influences of cluster size (the heterojunction dimension) on the electrochemical stability/activity (particularly the CO poisoning) of the $Pt_S/Ru_C$ NCs. To prove the corresponding mechanisms, NCs comprising 1.5 atomic layer Pt shell and ~3.0 nm Ru core were synthesized as substrates. Gold clusters having subnanometer size were intercalated at the interfacet corner sites atop the Pt shell. Our results combining DFT calculation, high-resolution transmission electron microscopy (HRTEM), temperature-programmed reduction (TPR), X-ray characterizations (including X-ray absorption spectroscopy, X-ray photoemission, and small-angle X-ray scattering), and CO stripping demonstrated that the gold clusters extract a substantial extent of electron injection from core to shell region. These electrons form the negatively charged corner regions that weaken the CO chemisorption at the NC surface. The intercalation by Au clusters induces the atomic distance displacement at NCs. These charactertics enable highly stable NCs in direct methanol fuel cells. Details of the atomic structure of NCs related to the electrochemical performance of CO stripping are given in later sections.

## EXPERIMENTAL SECTION

**Materials.** Hexachloride platinum acid ($H_2PtCl_6{\cdot}6H_2O$, 99 at %) was obtained from Sigma-Aldrich. Ruthenium(III) chloride hydrate ($RuCl_3{\cdot}3H_2O$, 99.0%) was obtained from Strem. The poly(vinylpyrrolidone) stabilizer (PVP-40, MW ~ 42 000, 99%) was obtained from Sigma-Aldrich. $H_2SO_4$ (99.9%) and $HNO_3$ (99.9%) were obtained from Sigma-Aldrich. The reaction solvent (ethylene glycol, EG, >99.5%) was obtained from Fluka Co. Inc.

**Nanoparticle Preparation.** The $Ru_{core}$–$Pt_{shell}$ NCs (denoted as Au-0) were synthesized by a sequence-controlled multistep polyol method. The Ru core NPs were synthesized by reducing 100 mM ruthenium chlorite in ethylene glycol (EG) in the presence of 10 wt % poly(vinylpyrrolidone) (PVP) stabilizer at 160 °C for 2 h.[6] After that, the Pt shell in 1.5 monolayer atoms was produced at the Ru core by a thermal reduction of Pt anions ($H_2PtCl_6{\cdot}6H_2O$, 15 mM) in EG at 160 °C for 2 h. The atomic-scaled gold clusters having different sizes intercalated at the corner sites of $Pt_SRu_C$ NCs by reducing the gold cations with atomic ratios of Au/Pt = 0.05 and 0.15 in the subsequent polyol reaction, where the corner sites of NCs served as nuclei for growing the Au clusters. The resulting NCs with Au/Pt = 0, 0.05, and 0.15 are denoted as Au-0, Au-05, and Au-15, respectively. In this step, the conditions of the polymer stabilizer and thermal process were set to be the same as that employed in previous steps. The surface compositions of the NCs were determined by using XPS analysis, and the results are given in Figure S1 of Supporting Information (SI).

**Catalyst Characterizations.** Nanostructure (shape, average particle size, and core–shell dimensions) of the NCs was determined by small-angle X-ray scattering (SAXS) analysis; data were collected at beamline of BL-23A at NSRRC (Taiwan). The valence band spectrum of the NCs was collected at beamline of BL-24A1 at NSRRC. The atomic structure and surface morphology of the NCs were determined by using high resolution transmission electron microscopy (HRTEM, FEI E.O Tecnai F20 G2 MAT S-TWIN field emission gun transmission electron microscope) at Electron Microscopy Center, Joint Laboratory of National Sun Yat-Sen University. The acceleration voltage for the electron beam was set to be 200 kV. To collect the atomic resolution images, the NCs were dispersed in dehydrated methanol and dropped on a 200 mesh copper grid having a glassy carbon support.

The anodic CO stripping measurement was conducted to evaluate the anti-CO poisoning capability and the CO sorption behavior for the experimental NCs; the corresponding index (the electrochemical surface area of CO sorption, $ECSA_{CO}$) can be determined by eq 1:

$$\mathrm{ESCA_{CO}} = \frac{Q_{CO}}{4.2\ \mathrm{C\ m^{-2}}\cdot g_{Pt}} \quad (1)$$

where $Q_{CO}$ is the experimental stripping charge (in C) determined after desorption of CO and 4.2 C $m^{-2}$ corresponds to an assumed charge associated with the oxidation of a monolayer of adsorbed CO.

The catalyst ink was prepared by using conventional approaches.[12,13] To prepare the CO stripping electrode, 10 $\mu$L of the ink slurry was spread on the surface of a glassy carbon electrode. For the CO voltammetric stripping experiments, the catalyst-loaded electrode was embedded in CO-saturated 0.1 M $HClO_4$ for 20 min with an applied voltage at 0.1 to adsorb CO atop the NC surface. Afterward, the experimental electrodes were transferred to $N_2$-saturated $HClO_4$ solution (0.1 M) for the subsequent CO stripping study. Two CV scans were collected between 0 and 1.2 V at a scan rate of 50 mV $s^{-1}$. The first potential sweep was conducted to electro-oxidize the adsorbed CO, and the second sweep was to verify the complete oxidation of the adsorbed species. The effects of Au cluster size on the surface oxidation state of the NCs were determined by TPR analysis. The details for the characterization methods and instrumental parameters are reported in the literature.[13]

**Density Functional Theory Calculations.** The theoretical analysis of first-principle calculations and analysis were performed by using Vienna ab initio simulation package (VASP)-based DFT calculation.[14] The projector-augmented wave (PAW) potentials were used to describe the core electrons. Generalized gradient approximation (GGA) in the form of a Perdew–Burke–Emzerhof (PBE) functional is adopted to describe the exchange correlation functional, which is developed for the calculation of surface systems.[14] The impact of Au clusters on the charge density of the Pt shell crystal was simulated by a repeating supercell model comprising three layers of a Ru(0001) facet in a 3 × 3 slab underneath 1.5 atomic layers of Pt atoms (packing in (111) facet symmetry) with a Au cluster (with three to nine atoms) intercalated at the corner sites. In these calculations, the vacuum region was set to 30 Å to minimize the potential interference between top and bottom surfaces on the periodic slabs. A kinetic energy cutoff of 300 eV for the plane wave basis was used. Finally, the cutoff plane wave expansion was taken to be 300 eV and the Monkhorst–Pack mesh of $k$-points for the irreducible Brillouin zone (IBZ) was chosen to be 2 × 2 × 1. The structure was optimized until the energy and net force on every atom were smaller than $10^{-5}$ eV and 0.025 eV $Å^{-1}$, respectively.

## RESULTS AND DISCUSSION

**Nanostructure of the Nanocrystallites.** The nanostructure of NCs (the surface configurations and the crystal structure)



DOI: 10.1021/acs.jpcc.6b00801
J. Phys. Chem. C 2016, 120, 7621–7628

was determined by combining results from high resolution transmission electron microscopy (HRTEM). Figure 1 compares

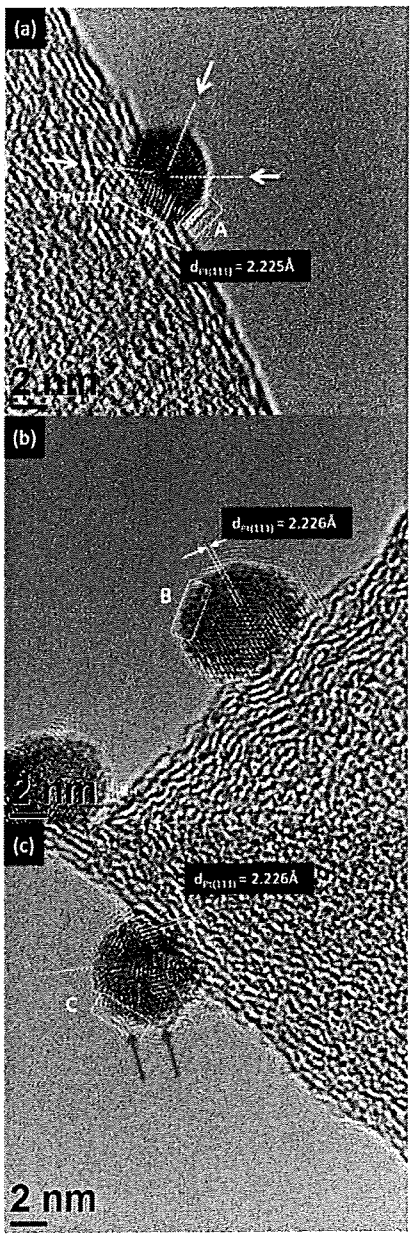


**Figure 1.** HRTEM images for samples of $Pt_S/Ru_C$ NCs intercalated by Au clusters in Au/Pt ratios of (a) 0, (b) 5, and (c) 15 at%.

the HRTEM images of Au-0 (**1a**), Au-05 (**1b**), and Au-15 (**1c**), respectively. According to Figure 1a, Au-0 is grown in multifaceted crystallites with twin boundaries (denoted by arrows in yellow) preferentially oriented at Pt(111) facets in different directions (denoted by arrows in white). The interplanar spacing ($d_{(111)}$) is determined to be 2.225 Å which is compressed by ~1.7%, compared with that of the Pt(111) facet for metallic Pt. This lattice compression is formed by allocating the Pt atoms atop the substrate of the Ru(0001) facet (which possesses the same atomic arrangement but with an interatomic distance relatively smaller than that of Pt(111)) and is aligned in the lateral direction in the shell crystal region. The atomic structure is well-ordered with kinks and steps at the particle surface (region A), consistently suggesting the formation of a semicoherent core–shell interface.[15] For the case of Au-05 (Figure 1b), $d_{(111)}$ remains unchanged. However, the atomic disorder is evident at the NC surface (see region B). This phenomenon can be caused by spontaneous transmetalation between Au anion and metallic Pt atoms followed by the relaxation of lattice and atomic restructures.[10] By increasing the Au/Pt ratio to 15 at% (Au-15 in Figure 1c), considerable reconstruction was found in the presence of subnanometer clusters (denoted by arrows in red in region C) at the NC surface. In this case, the twin boundaries did not intersect at the same position. This indicates that they are formed by intersection of the Au clusters at the heterojunction between interfaceted regions at the Pt shell crystal. These unique atomic clusters will trigger a strong lattice strain and atomic distance displacement which not only reinforce the atomic structure stability during the long-term MOR reaction but suppress the chemisorption of carbonaceous molecules (particular the CO molecule in our case) at the binuclear (bridge) or trinuclear (hollow) sites in the shell region.

The structure parameters of core–shell NCs (including $D_{avg}$, Schulz distribution of particle size ($P_R$), shell thickness ($T_S$)) and the intercalated Au clusters were determined by SAXS analysis. The SAXS spectra [$I(Q)$ vs $Q$] and the obtained Schulz distributions of particle size for the experimental NCs are shown in Figure 2a and 2b, respectively. In general, the features of SAXS spectra originate from the interference from incident X-ray photons that are scattered between interparticle correlations (i.e., the structure factor in $Q < 0.07$ Å$^{-1}$ ($S(Q)$), the interparticle distance, and the size of the particle agglomerates) and the intraparticle correlations of the NCs (i.e., the form factor in $Q > 0.07$ Å$^{-1}$ ($P(Q)$), the shape, the dimension of core/shell regions, and the dimensions of Au clusters). Considering the shape and architecture of the experimental NCs, the SAXS spectra of Au-intercalated NCs were described by the contributions from fractal aggregate and core–shell cylindrical models with an external factor from the Au cluster (see eq 2 for Au-05 and Au-15).[16−18]

$$I(Q) = A^{F}S(Q)^{F}P(Q)^{F} + A^{CS_C}S(Q)^{CS_C}P(Q)^{CS_C} \quad (2)$$

where $A$ is the number density of the scattering objects. Both $S(Q)$ and $P(Q)$ are a function of the momentum transfer ($Q$) between incident and scattered X-rays. $Q$ is given by $Q = (4\pi/\lambda) \times \sin(\theta/2)$ in an elastic scattering process, where $\theta$ denotes the angle between the incident and scattered beams at a wavelength of $\lambda$.

The scheme for scattering wave pathways of core–shell NCs with and without Au clusters is shown in Figure 2c. For NCs without Au clusters, the superscripts F (fractal) and the CS_C (core–shell cylinder) refer to the model associated with the parameter. For the case of NCs with Au clusters (Au-05, Au-10), the interfering X-rays originate from both the outermost surface of the Au clusters and from the intraparticle interface (i.e., the core–shell interface and the cluster to the NC interface as denoted by arrow I). In this circumstance, the scattered X-rays at Au clusters contribute to the diffusion scattering background (denoted by arrows II), where the interparticle scattering correlation factors ($A^F$, $S(Q)^F$, and $P(Q)^F$) are modified into the intercluster ones and represented by $A^{Fclu}$, $S(Q)^{Fclu}$, and $P(Q)^{Fclu}$. The fitting curves of the proposed model are compared



DOI: 10.1021/acs.jpcc.6b00801
J. Phys. Chem. C 2016, 120, 7621−7628

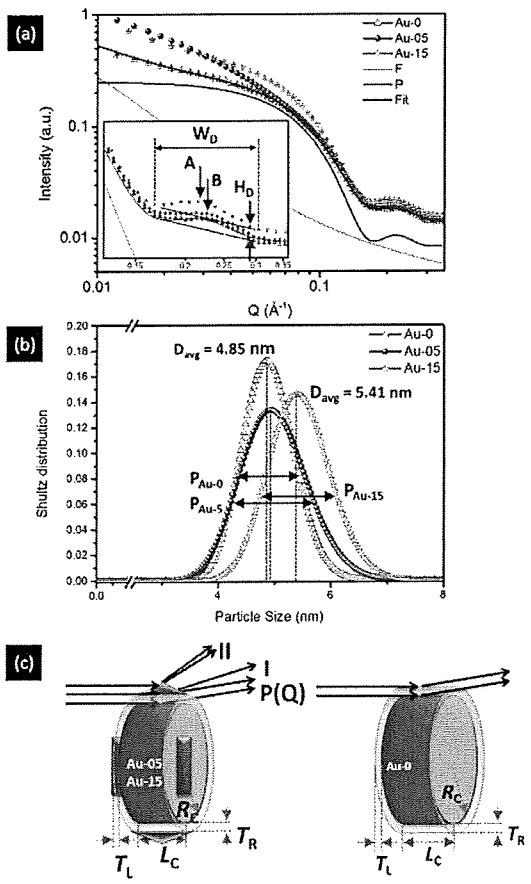


Figure 2. (a) SAXS spectra of the $Pt_S/Ru_C$ NCs intercalated by Au clusters in Au/Pt ratios of 0 to 15 at%, (b) the corresponding particle size distributions, and (c) the scheme for scattering waveforms at core–shell nanoparticles (left) with and (right) without Au clusters atop.

with that of the SAXS spectra of experimental NCs in Figure 2a, and the obtained structure parameters are summarized in Table S1, SI. In our study, only the intraparticle structure parameters (in the high Q region, $Q > \sim 0.1$ Å$^{-1}$) are discussed. This is because the electrochemical activity of NCs are dominated by intraparticle structure parameters including the heteroatomic distribution, the shape, and the size of the particle. In the high Q region, the position ($Q_X$) with the width ($W_D$)/height ($H_D$) of the first scattering hump is the contributions of particle sizes (or the aspect ratio of longitude and latitude axes) and intraparticle boundaries (i.e., scattering within the core crystal body and between the core–shell interface and the outermost surface of the NCs) to the SAXS spectrum, where $W_D/H_D$ ratio is proportional to the roughness of core–shell (shell-solvent) interfaces and the polydispersity ($\eta$) of the core diameter ($D_{core}$) and shell thickness ($T_{shell}$), respectively. As shown in Figure 2a inset, the downshift of the oscillation hump from B to A elucidates the increasing phase divergence of interference between the Au cluster to surface Au–Pt interface scattering (arrows I and II in Figure 2c) and the increasing cavity length (the shell thickness, $T_S$) with Au/Pt ratios from 0 to 15%. The geometry of the Au clusters was further illustrated by comparing the $\eta$ and $D_{avg}$ of the experimental NCs in Figure 2b. As revealed, the $D_{avg}$ and $\eta$ of Au-0 is determined to be 4.85 nm and 9.4%, respectively. For Au-05 NCs, the surface to bulk ratio of 5 nm NCs is estimated to be ~60% from geometry understandings. This means that the Au atoms cover ~1/4 of the surface area, therefore growing the particle diameter by 0.15 nm (0.25 × 2 atomic layers. The corresponding atomic packing is given in Scheme S1, SI. However, by increasing the Au/Pt ratios to 15% the $D_{avg}$ is grown by 0.6 nm (i.e., two atomic layers in thickness) to ~5.41 nm. This feature indicates that the Au atoms tend to intercalate at the interfacet corner sites via a heterogeneous crystal growth pathway at layer-plus-island mode. As consistently shown by the scattering model in Figure 2c, the incident X-rays will be scattered into different phases by the highly rough surface of the NCs having large Au clusters and increase the $\eta$ to 11.2%.

**Effects of Au Cluster Size on the Surface Oxidation and CO Poisoning of NCs.** Figure 3a compares the TPR spectra of

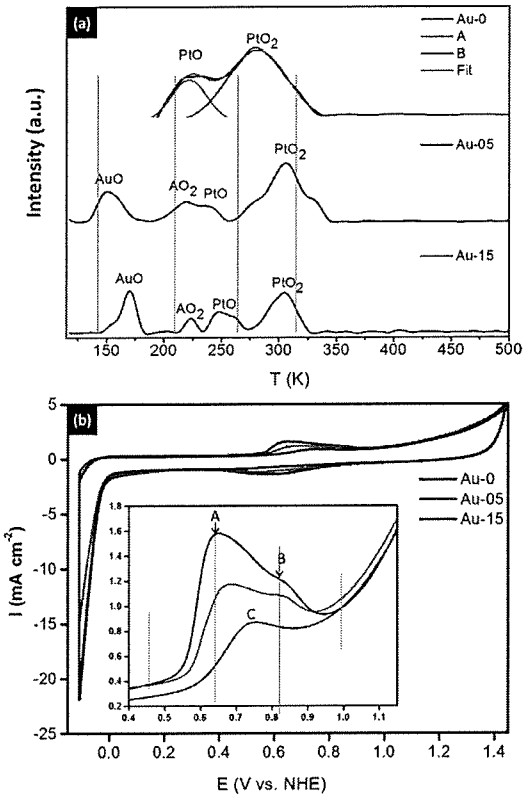


Figure 3. (a) Temperature-programmed reduction curves and (b) CO stripping curves of $Pt_S/Ru_C$ NCs intercalated by Au clusters in Au/Pt ratios of 0, 5, and 15 at%.

the experimental NCs. For Au-0 NCs, the two strong peaks A (at 220 K) and B (at 281 K) are characteristic for $H_2$ consumption by interacting with PtO and $PtO_2$ species, respectively.[13] The strong peak intensity indicates considerable oxidation of Pt atoms in the shell region. By intercalating Au atoms with Au/Pt = 5 atom %, the intensity of peaks A and B are greatly suppressed and the positions are shifted to the high temperature side accompanied by the presence of a broad reduction peak at 150 K for AuO and 224 K for PtAu alloy oxide ($AO_2$). These features directly elucidate the protection of the Pt shell from oxidation by capping with Au clusters. By increasing Au/Pt to 15 at%, the Pt oxide species are further suppressed by 50% or more. The upshift of the AuO peak from 150 to 170 K implies the shielding of low energy Pt–O adsorption sites by Au atoms. Moreover, when compared



DOI: 10.1021/acs.jpcc.6b00801
J. Phys. Chem. C 2016, 120, 7621–7628

with Au-0 catalysts, the narrowing of the reduction peaks again suggest the preferential intercalation of Au atoms at the kink or step sites of the outermost region in the Pt shell of Au-05 and Au-15.

The effects of Au cluster size on the CO poisoning of the core–shell NCs were revealed by CO stripping analysis. The CO stripping voltammograms of the experimental NCs are compared in Figure 3b. A full sweep at potentials up to 1.42 V (vs NHE) causes substantial water oxidation and consequently OH reduction in the low potential region (from 0.12 to 0.10 V vs NHE). In general, the position and areas of CO oxidation peaks in the CV curves indicate (also the required voltage to drive the maximum CO oxidation kinetics) the identity and the relative amount of surface sites that have been occupied by CO chemisorption. As indicated for Au-0, the CO oxidation region (0.45 to 1.00 V vs NHE) comprise two oxidation peaks at ca. 0.63 V (peak A) and ca. 0.82 V (peak B). In these CV sweep curves, because all the NCs were supported by identical material (FTO), the effects of the interface contact and the residual capacitance can be ruled out on the basis of the CO chemisorption behavior with the experimental NCs. In this case, the electro-oxidation peaks can be attributed to CO chemisorption at surface sites with different binding energies, where peaks A and B are related to the sorption of CO at close packed (low sorption energy) and opened (high sorption energy) facets, respectively. For Au-05 NCs, the two substantially suppressed CO peaks confirmed the Au shielding at the Pt shell surface. By further increasing Au to 15 at%, the peak B faded away and the position of peak A shifted to the high potential side. These characteristics indicate the modification of CO sorption energy by the electron injection and the dangling bond coverage around the Pt sites (at interfacet kink or step regions) by Au clusters with an interface lattice mismatch in between. Previous studies have proved that CO sorption energy at the Pt site is weakened by the compressive lattice strain in the shell crystal, where Pt atoms donate valence electrons to neighboring atoms.[2,11,15] In this work, we demonstrated that the electron injection was triggered from Pt to Au sites as indicated by the upshift of the onset potential ($V_{OC}$) of the CO oxidation peak of Au-05 and Au-15 compared to that of Au-0. The downshift of the potential for initiating the surface electrochemical reaction on NCs is consistently proved by DFT calculation on the surface potential of NCs.[19] Accordingly, the Au clusters drain the electrons from Pt and Ru domains by introducing external expansive lattice strain atop the Pt shell crystal.[15]

The shielding effects of Au clusters on NC surface oxidation were further elucidated by using X-ray absorption spectroscopy. The Pt $L_3$-edge Fourier-transformed extended X-ray absorption fine structure (EXAFS) spectra for the experimental NC samples are compared in Figure 4, where the three radial peaks A, B, and C are contributions of chemisorption oxygen (peaks A and C) and metallic Pt atoms (peak B) around the Pt center, respectively, suggesting that these NCs consist of metallic Pt and PtOx. Compared with Au-0, the intensity of radial peak A of Au-05 is decreased by ~7%, indicating suppressed oxygen chemisorption atop the Pt shell crystal by the incorporation of Au clusters. In this case, the substantial enhancement of peaks B and C is a consequence of the increasing Pt–Pt bond pairs by capping with Au clusters. By increasing the Au/Pt ratio to 15 at%, the intensity of peak A for Au-15 is further reduced to less than 40% of that of Au-0, again confirming the strong shielding capability of Au clusters atop the Pt shell crystal. In this circumstance, the intensity of metallic radial bonds (peaks B and C) are reduced by

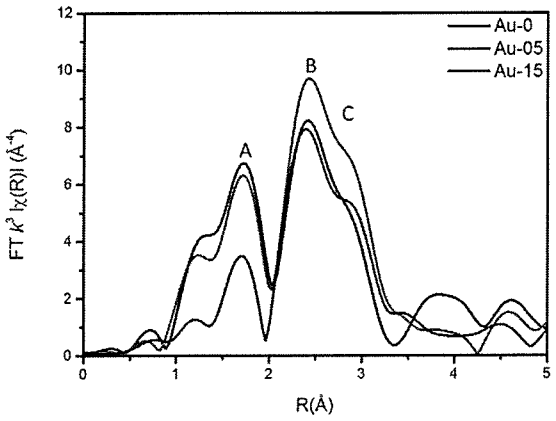


**Figure 4.** Fourier-transformed EXAFS spectra (radial structure function, RSF) of $Pt_S/Ru_C$ NCs intercalated by Au clusters in Au/Pt ratios of 0, 5, and 15 at%. (the corresponding fitting curves are given in Figure S2, SI). Peaks A, B, and C are contributions of chemisorption oxygen (peaks A and C) and the metallic Pt atoms (peak B) around the Pt center, respectively.

~18% compared with that of Au-05. This unique feature can be attributed to the increasing out-of-phase X-ray interference due to the local disordering around Pt atoms by the considerable Au intercalation at interfaceted regions (as consistently revealed by HRTEM analysis in Figure 1).

The quantitative structure parameters were determined by atomic model fitting, and the results are summarized in Table 1.

**Table 1. X-ray Absorption Spectroscopy Determination of Structure Parameters of $Pt_S/Ru_C$ NCs Intercalated by Au Clusters in Au/Pt Ratios of 0, 5, and 15 at%[a,b]**

| NC | phase | bond pair | R | CN[c] |
|---|---|---|---|---|
| Au-0 | PtOx | Pt–Oox | 2.068 | 2.67 |
| | | Pt–Ptox1 | 2.878 | 2.67 |
| | | Pt–Ptox2 | 3.266 | 5.35 |
| | PtM | Pt–Pt | 2.751 | 6.06 |
| Au-05 | PtOx | Pt–Oox | 2.068 | 2.23 |
| | | Pt–Ptox1 | 2.858 | 2.23 |
| | | Pt–Ptox2 | 3.246 | 4.47 |
| | PtM | Pt–Pt | 2.751 | 6.83 |
| Au-15 | PtOx | Pt–Oox | 2.053 | 1.02 |
| | | Pt–Ptox1 | 2.839 | 1.02 |
| | | Pt–Ptox2 | 3.227 | 2.04 |
| | PtM | Pt–Pt | 2.742 | 5.63 |

[a]The *R* factor of all fitting results are constrained to smaller than 0.01. [b]The sigma square of all bond pairs are set to the same value obtained from fitting results of standard Pt foil. [c]CN: coordination number.

For the case of Au-0 NCs, the coordination number (CN) of Pt–O, Pt–Ptox1/Pt–Ptox2, and Pt–Pt is determined to be 2.67, 2.67/5.35, and 6.06, respectively. Compared with that of the theoretical model, the CN of oxide and metal bond pairs is reduced by ~33% and ~50%, respectively, indicating the coexistence of metallic Pt and Pt with oxygen chemisorption in the near surface region of Au-0. By increasing the Au/Pt ratio to 0.05, the CNs of Au-05 at bond pairs of the Pt oxide phase are reduced by ~16.5% (while CN of the Pt metal phase is increased by 12.7%) compared with that of Au-0. It again reveals the protection of NCs from oxidation by Au clusters. For the Au-15



DOI: 10.1021/acs.jpcc.6b00801
J. Phys. Chem. C 2016, 120, 7621–7628

NCs, the CN at bond pairs of Pt oxides is substantially reduced by ~61.7%. Considering the geometry effects of Au clusters as shielding, a further increment in the metallic phase bond pair intensity is expected by growing the Au cluster size. However, it turns out that the CN of the Pt metal bonds for Au-15 is reduced by ~7.1% compared with Au-0. These controversial results can be explained by the local distortion at the Pt shell crystals. Given that the thickness of Pt shell atoms is ~1.5 atomic layers in our NCs, our fitting results imply that all the Pt atoms are exposed to ambient environments for Au-0. In ideal conditions, six metallic Pt atoms and three oxygen atoms are found around the surface Pt atoms in lateral and out of plane regions, respectively. The slight decrease in Pt–O could be attributed to the geometric loading effects of Pt atoms that exceed a single monolayer atop the Ru core. In this circumstance, the significantly reduced CN on both Pt–O and Pt–Pt bond pairs is strong evidence for both shielding and local distortion on the Pt shell crystal.

The Ru K-edge RSF spectra of the Au-0, Au-05, and Au-15 NCs (annealed at 330 °C for 30 min) are compared in Figure S3, SI. As indicated, the two radial peaks A and B are contributions of Ru–O and Ru–Ru bond pairs in oxide and metal phases, respectively. For Au-0 NCs, the considerable intensity of peak A can be attributed to the slight oxidation at the core–shell interface where certain amounts of Ru atoms were exposed to the outermost layer due to relocation between Pt shell and Ru core atoms during annealing. Increasing the Au/Pt ratio to 5 at% (Au-05) suppresses/enhances peak A/B which again demonstrates the shielding effects of Au clusters in the NCs. Increasing the Au/Pt ratio to 15 at% (Au-15) further suppresses peak A. In the meantime, the decrease in peak B intensity is attributed to the slight modification of atomic structure of the Ru core domain. As consistently observed by RHTEM in Figure 1c, this phenomenon rationalizes the strong lattice distortion at the core–shell interface due to the presence of large size Au clusters atop the $Pt_S/Ru_C$ NPs.

**Clues for Au Atomic Shielding on the Valence Band Structure of NCs.** The intercalation by Au clusters results in several functions: (1) capping/protecting defect sites from oxidation; (2) adding heterojunctions atop to drain electrons to the outermost region of core–shell NCs; (3) reinforcing defect sites from restructuring; (4) protecting active sites from CO poisoning on elctrocatalysts in the operando fuel cell or in electrochemical devices. As shown in previous works,[11] these functions are most likely triggered by the geometry atomic stacking effects and the strong negative charge dipole between Au clusters and the embedded Pt crystal. The results of valence band (VB) photoemission spectroscopy (VB) demonstrated that the proposed shielding effects are mainly dominated by charge donation from Pt to Au by the localized interface lattice strain as well as the electronegative dipole.

The VB spectra of experimental NCs (Au-0, Au-05, and Au-15) are shown in Figure 5. There are several typical features regarding the electron distribution in the VB spectrum of Au-0 NCs including the following: (region A) a cliff from 0.00 to ~0.80 eV with the tangent line at the Fermi level ($E_F$), a slide with a reflection point at ~1.15–1.20 eV (i.e., the surface $E_b$), and a slide till ~3.40 eV (denoted by arrow X); (region B) a broad peak ranging from 3.40 to 11.80 eV; (region C) a shoulder rising from 11.80 eV till 14.00 eV. These features clarify the effects of interface lattice strain and the heteroatomic arrangements on the valence electronic configuration of NCs. In region A, the decreasing VB intensity indicates the lowered density of states (DOS) at the outermost band. As resolved by DFT calculation in

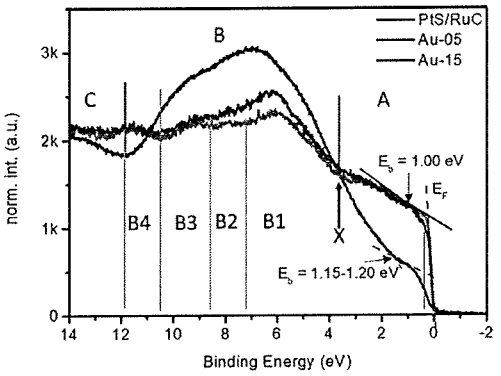


**Figure 5.** Valence band spectra of $Pt_S/Ru_C$ intercalated by Au clusters in Au/Pt ratios of 0, 5, and 15 at%.

a later section, this phenomenon can be attributed to the charge redistribution from Pt to the neighboring oxygen atoms due to the interfacial lattice strain and the metal–oxygen bond.[8,15] The opened DOS tends to attract electrons from chemisorbed molecules, and the high intensity broad band in region B builds a negative charge at the NC surface. The former lowers the activation energy of chemisorption, and the latter prohibits the retention of electronegative molecules/ligands (e.g., CO or CHO:). These features facilitate the redox activity and improve the long-term redox stability (by preventing the poisoning of reaction sites) of the NCs. Region C denotes the photoemission current near the core level. Compared to that of Au-0, the photoemission current in region A increases with the Au content till 15 at% (Au-15). This indicates the preservation of valence charge at the outermost band by the protection of Pt atoms and the strain-induced charge relocation to the subnano Au clusters at the interfaceted region of the shell crystal. The Au-induced electron relocation to the near-Fermi level region was consistently elucidated by changes to the VB feature in region B. In this region, the bandwidth is expanded to 10.90 eV and splits into B1, B2, B3, and B4 centered at 6.1, 8.0, 9.1, and 11.8 eV, respectively. These distinct features refer to the photoemission lines of metallic Pt at varied facets. The increasing intensity from B4 to B1 indicates the relocation of core level electrons to the valence band. This shows a strong electron extraction force from the Au clusters at the shell region, increasing with the Au content from 5 to 15 at%. In region C, the higher photoemission current indicates the preservation of valence electrons near core level regions owing to the weaker extent of strain-induced electron injection compared with that of Au-05 and Au-15. In addition, compared to the band structure of Au-0, the split bands refer to a strong electron repulsive force in the valence band and can be attributed to the inductive local compressive strain in the shell crystal from the intercalation by the Au cluster.

The inductive charge relocation is further evidenced by the DFT calculated charge density distribution of the atomic model of $Ru@Pt–Au^{cluster}$. In Figure 6, the black dashed parallelogram represents the supercell of the Ru(0001)@Pt model intercalated with the Au cluster; cyan, orange, and yellow spheres represent Ru, Pt, and Au atoms, respectively. Red and blue isosurfaces represent depletion (−) and addition (+) of the induced charge 0.02 $lel/A^{-3}$ upon Au doping. The induced charge density (right-hand side) was determined by subtracting the charge density of the optimized Au cluster-intercalated Ru(0001)@Pt with that of



DOI: 10.1021/acs.jpcc.6b00801
J. Phys. Chem. C 2016, 120, 7621–7628

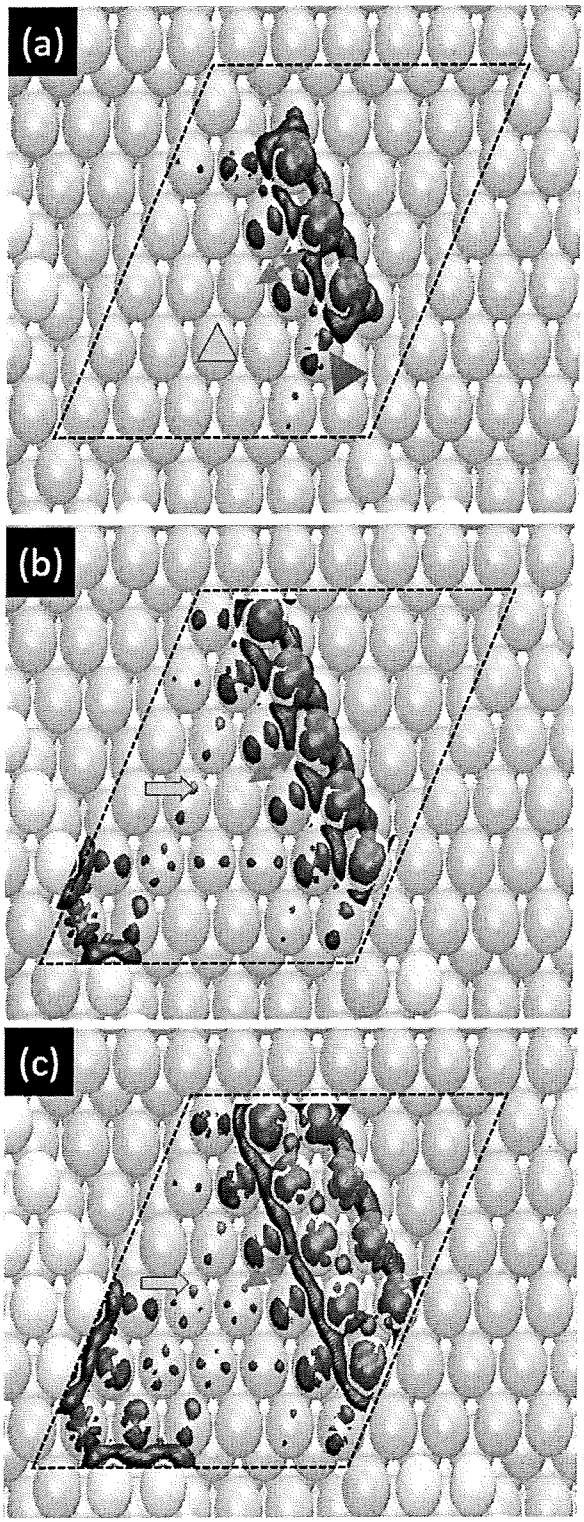


Figure 6. DFT-simulated electron density distribution of 3 × 3 Ru(0001) slab underneath 1.5 layer Pt atoms with (a) three, (b) five, and (c) nine Au atoms intercalated at the edge site.

the isolated Au cluster and Ru(0001)@Pt. The induced charge distributions of models with Au clusters containing three, five, and nine atoms are demonstrated in Figure 6a, 6b, and 6c, respectively. Accordingly, a large charge separation (denoted by double arrows in blue in Figure 6) was found at the Pt atoms adjacent to the Au clusters. In addition, the depletion regions (denoted by the isosurface in red) with the charge localization (concentration) were found around and at the center of the Au atoms in the cluster. These features suggest impacts of local lattice strain and the electronegative dipole between the Au cluster and the Pt domain at the kink region. By increasing the number of Au atoms, the charge localization at the cluster, the depletion area at the interface and on the outermost layer Pt region (denoted by arrow in green in Figure 6b and 6c), and the charge separation at the Pt atoms adjacent to Au are progressively enhanced. These features complement the results of CO stripping analysis which clarify the effects of Au cluster size on the sorption behavior of CO (electronegative molecules) atop $Pt_S/Ru_C$ NCs. For the case of NCs with a three Au atom cluster, the charge localization and separation region is limited in the Au cluster and the neighboring atoms, therefore resulting in two types of sorption sites with and without charge localization (denoted by blue and green triangles in Figure 6a) for CO chemisorption. By increasing the number of Au atoms, the depletion region progressively expands from the cluster interface to the Pt bulk. This illustrates the electron extraction from substrate by the strong electronegativity of Au as well as the local expansion strain around Au atoms in the shell region (Figure 6b and Figure 6c). This driving force synchronizes the chemical state of Pt sites to a certain extent. As consistently proved by CV stripping results, the two CO stripping peaks in Figure 3b merged into peak C with a substantial intensity suppression consistently indicating the weakened CO chemisorption by increasing Au/Pt ratios. The impacts of the Au cluster on charge relocation at the valence band of the Ru(0001)@Pt model are further confirmed by the DFT calculation with a work function shift in SI (Figure S7).

## ■ CONCLUSION

The effects of atomic scaled gold clusters atop $Pt_{shell}$–$Ru_{core}$ NCs were elucidated by combining the results of structural characterizations, electrochemical CO stripping, and ab initio first principle DFT calculations. We found that these clusters reduced the oxidation current of carbon monoxide to a maximum extent of ~53% by increasing the Au/Pt ratios from 0 to 15 at%. Such substantial improvement is caused by steric shielding and electron extraction by Au atoms at the NC edge sites. These Au atoms form a prevailing electron field and a local distortion of sorption sites in the near surface region that rejects the sorption of electronegative ligand/molecules on the NCs. Most importantly, a robust assessment with mechanistic insights was provided for synthesizing nanoscaled heterojunction NCs as chemically durable anodes for fuel cell applications.

## ■ ASSOCIATED CONTENT

### Supporting Information

The Supporting Information is available free of charge on the ACS Publications website at DOI: 10.1021/acs.jpcc.6b00801.

Methods for SAXS data collection, analysis, and instruments. Fitting curves of EXAFS spectra. XPS spectra of experimental samples (PDF)



DOI: 10.1021/acs.jpcc.6b00801
J. Phys. Chem. C 2016, 120, 7621–7628

## AUTHOR INFORMATION


### Corresponding Authors

*E-mail: chencaeser@gmail.com. Tel: +886-3-5742671. Fax: +886-3-5728445.

*E-mail: yliu@nchu.edu.tw.


### Notes

The authors declare no competing financial interest.

## ACKNOWLEDGMENTS

The authors thank the staff of National Synchrotron Radiation Research Center (NSRRC), Hsinchu, Taiwan, for help with various synchrotron-based measurements. The VASP-based DFT simulation was conducted by Prof. Horng-Tay Jeng's group using clusters at Department of Physics at National Tsing Hua University. T.-Y. Chen acknowledges the funding support from research projects of the National Tsing Hua University, Taiwan (N103K30211 and 103N1200K3), and the Ministry of Science and Technology, Taiwan (MOST 103-2112-M-007-022-MY3). Y.-T. Liu acknowledges the funding support from research project of Ministry of Science and Technology, Taiwan (MOST 104-2311-B-005-016-MY3).

## REFERENCES


(1) Sasaki, K.; Naohara, H.; Cai, Y.; Choi, Y. M.; Liu, P.; Vukmirovic, M. B.; Wang, J. X.; Adzic, R. R. Core-Protected Platinum Monolayer Shell High-Stability Electrocatalysts for Fuel-Cell Cathodes. *Angew. Chem., Int. Ed.* **2010**, *49*, 8602−8607.

(2) Alayoglu, S.; Nilekar, A. U.; Mavrikakis, M.; Eichhorn, B. Ru−Pt Core−shell Nanoparticles for Preferential Oxidation of Carbon Monoxide in Hydrogen. *Nat. Mater.* **2008**, *7*, 333−338.

(3) Hogarth, M. P.; Ralph, T. R. Catalysis for Low Temperature Fuel Cells. *Platinum Met. Rev.* **2002**, *46*, 117−135.

(4) Watanabe, M.; Motoo, S. Electrocatalysis by Ad-Atoms: Part III. Enhancement of the Oxidation of Carbon Monoxide on Platinum by Ruthenium Ad-Atoms. *J. Electroanal. Chem. Interfacial Electrochem.* **1975**, *60*, 275−283.

(5) Schlapka, A.; Lischka, M.; Gross, A.; Kasberger, U.; Jakob, P. Surface Strain Versus Substrate Interaction in Heteroepitaxial Metal Layers: Pt on Ru(0001). *Phys. Rev. Lett.* **2003**, *91*, 016101.

(6) Chen, T.-Y.; Lin, T.-L.; Luo, T.-J. M.; Choi, Y.; Lee, J.-F. Effects of Shell Thicknesses on the Atomic Structure of Ru-Pt Core-Shell Nanoparticles for Methanol Electrooxidation Applications. *ChemPhysChem* **2010**, *11*, 2383−2392.

(7) Long, N. V.; Yang, Y.; Thi, C. M.; Minh, N. V.; Cao, Y.; Nogami, M. The Development of Mixture, Alloy, and Core-Shell Nanocatalysts with Nanomaterial Supports for Energy Conversion in Low-Temperature Fuel Cells. *Nano Energy* **2013**, *2*, 636−676.

(8) Strasser, P.; Koh, S.; Anniyev, T.; Greeley, J.; More, K.; Yu, C.; Liu, Z.; Kaya, S.; Nordlund, D.; Ogasawara, H.; et al. Lattice-Strain Control of the Activity in Dealloyed Core−Shell Fuel Cell Catalysts. *Nat. Chem.* **2010**, *2*, 454−460.

(9) Wang, J.-J.; Liu, Y.-T.; Chen, I.-L.; Yang, Y.-W.; Yeh, T.-K.; Lee, C.-H.; Hu, C.-C.; Wen, T.-C.; Chen, T.-Y.; Lin, T.-L. Near-Monolayer Platinum Shell on Core−Shell Nanocatalysts for High-Performance Direct Methanol Fuel Cell. *J. Phys. Chem. C* **2014**, *118*, 2253−2262.

(10) Bligaard, T.; Nørskov, J. K. Ligand Effects in Heterogeneous Catalysis and Electrochemistry. *Electrochim. Acta* **2007**, *52*, 5512−5516.

(11) Chen, T.-Y.; Li, H.-D.; Lee, G.-W.; Huang, P.-C.; Yang, P.-W.; Liu, Y.-T.; Liao, Y.-F.; Jeng, H.-T.; Lin, D.-S.; Lin, T.-L. Gold Atomic Clusters Extracting the Valence Electrons to Shield the Carbon Monoxide Passivation on Near Monolayers Core-Shell Nanocatalysts in Methanol Oxidation Reactions. *Phys. Chem. Chem. Phys.* **2015**, *17*, 15131−15139.

(12) Huang, S.-Y.; Chang, C.-M.; Yeh, C.-T. Promotion of Platinum−Ruthenium Catalyst for Electro-Oxidation of Methanol by Ceria. *J. Catal.* **2006**, *241*, 400−406.

(13) Huang, S.-Y.; Chang, S. M.; Lin, C. L.; Chen, C. H.; Yeh, C.-T. Promotion of the Electrochemical Activity of a Bimetallic Platinum−Ruthenium Catalyst by Oxidation-Induced Segregation. *J. Phys. Chem. B* **2006**, *110*, 23300−23305.

(14) Chang, C.-P.; Chu, M.-W.; Jeng, H. T.; Cheng, S.-L.; Lin, J.-G.; Yang, J.-R.; Chen, C. H. Condensation of Two-Dimensional Oxide-Interfacial Charges Into One-Dimensional Electron Chains by the Misfit-Dislocation Strain Field. *Nat. Commun.* **2014**, *5*, 3522.

(15) Adzic, R. R.; Zhang, J.; Sasaki, K.; Vukmirovic, M. B.; Shao, M.; Wang, J. X.; Nilekar, A. U.; Mavrikakis, M.; Valerio, J. A.; Uribe, F. Platinum Monolayer Fuel Cell Electrocatalysts. *Top. Catal.* **2007**, *46*, 249−262.

(16) Teixeira, J. Small-Angle Scattering by Fractal Systems. *J. Appl. Crystallogr.* **1988**, *21*, 781−785.

(17) Guinier, A.; Fournet, G. *Small-Angle Scattering of X-Rays*; John Wiley and Sons: New York, 1955.

(18) Wagner, J. Small-Angle Scattering from Spherical Core−Shell Particles: An Analytical Scattering Function for Particles with Schulz−Flory Size Distribution. *J. Appl. Crystallogr.* **2004**, *37*, 750−756.

(19) Ma, J.; Habrioux, A.; Morais, C.; Lewera, A.; Vogel, W.; Verde-Gómez, Y.; Ramos-Sanchez, G.; Balbuena, P. B.; Alonso-Vante, N. Spectroelectrochemical Probing of the Strong Interaction between Platinum Nanoparticles and Graphitic Domains of Carbon. *ACS Catal.* **2013**, *3*, 1940−1950.




DOI: 10.1021/acs.jpcc.6b00801
J. Phys. Chem. C 2016, 120, 7621−7628